J. Fluid Mech. (2024), *vol*. 981, R2, doi:10.1017/jfm.2024.86

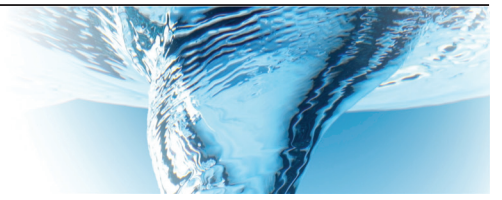

Transition to fully developed turbulence in liquid-metal convection facilitated by spatial confinement

Lei Ren[1], **Xin Tao**[1], **Ke-Qing Xia**[2] **and Yi-Chao Xie**[1,†]

[1]State Key Laboratory for Strength and Vibration of Mechanical Structures and School of Aerospace, Xi'an Jiaotong University, Xi'an 710049, PR China

[2]Center for Complex Flows and Soft Matter Research, Department of Mechanics and Aerospace Engineering and Department of Physics, Southern University of Science and Technology, Shenzhen 518055, PR China

(Received 3 December 2023; revised 17 January 2024; accepted 19 January 2024)

Using thermal convection in liquid metal, we show that strong spatial confinement not only delays the onset Rayleigh number Ra_c of Rayleigh–Bénard instability but also postpones the various flow-state transitions. The Ra_c and the transition to fully developed turbulence Rayleigh number Ra_f depend on the aspect ratio Γ with $Ra_c \sim \Gamma^{-4.05}$ and $Ra_f \sim \Gamma^{-3.01}$, implying that the stabilization effects caused by the strong spatial confinement are weaker on the transition to fully developed turbulence when compared with that on the onset. When the flow state is characterized by the supercritical Rayleigh number Ra/Ra_c (Ra is the Rayleigh number), our study shows that the transition to fully developed turbulence in strongly confined geometries is advanced. For example, while the flow becomes fully developed turbulence at $Ra \approx 200Ra_c$ in a $\Gamma = 1$ cell, the same transition in a $\Gamma = 1/20$ cell only requires $Ra \approx 3Ra_c$. Direct numerical simulation and linear stability analysis show that in the strongly confined regime, multiple vertically stacked roll structures appear just above the onset of convection. With an increase of the driving strength, the flow switches between different-roll states stochastically, resulting in no well-defined large-scale coherent flow. Owing to this new mechanism that only exists in systems with $\Gamma < 1$, the flow becomes turbulent in a much earlier stage. These findings shed new light on how turbulence is generated in strongly confined geometries.

Key words: Bénard convection, turbulent convection

† Email address for correspondence: yichao.xie@xjtu.edu.cn

1. Introduction

Thermally driven turbulence in liquid metal occurs widely in geophysical and astrophysical systems (Lohse & Shishkina 2023), e.g. in the outer core of the Earth, the convection of liquid iron is believed to be responsible for the generation of Earth's magnetic field (Glatzmaier *et al.* 1999). In these systems, the stabilizing forces produced by rotation or magnetic field are always found to inhibit turbulence (Chandrasekhar 1961), leading to unexpected enhancement of heat transport (see e.g. Zhong *et al.* 2009; Lim *et al.* 2019). Recent studies demonstrate that the stabilizing force introduced by spatial confinement in thermal turbulence shows surprisingly similar behaviour as the dynamic constraint by rotation, leading to condensation of the coherent structures and unexpected heat transport enhancement (Huang *et al.* 2013; Chong *et al.* 2017; Xia *et al.* 2023). It thus becomes essential to understand how the stabilization effects generated by spatial confinement alter the flow-state evolution, especially the transition to fully developed turbulence in liquid-metal convection.

The classical Rayleigh–Bénard convection (RBC) system is usually employed as a model system to study thermally driven flow. It contains a horizontally infinite fluid layer heated from below and cooled from above (for reviews, see e.g. Ahlers, Grossmann & Lohse 2009; Lohse & Xia 2010; Chillá & Schumacher 2012; Xia 2013). The system is governed by the Oberbeck–Boussinesq equations and the continuity equation below:

$$\frac{\partial \boldsymbol{u}}{\partial t} + (\boldsymbol{u}\cdot\boldsymbol{\nabla})\boldsymbol{u} = -\boldsymbol{\nabla} p + \sqrt{\frac{Pr}{Ra}}\nabla^2\boldsymbol{u} + T\hat{z}, \quad \frac{\partial T}{\partial t} + (\boldsymbol{u}\cdot\boldsymbol{\nabla})T = \sqrt{\frac{1}{RaPr}}\nabla^2 T, \quad \boldsymbol{\nabla}\cdot\boldsymbol{u} = 0. \tag{1.1a–c}$$

The equations (1.1*a–c*) have been made dimensionless using the cell height H, the temperature difference across the cell ΔT, the free-fall velocity $u_{ff} = \sqrt{\alpha g \Delta T H}$ and the free-fall time scale $\tau_{ff} = H/u_{ff}$. Here $\boldsymbol{u}$, p and T are the velocity vector, pressure and temperature, respectively. The vertical unit vector is denoted as $\hat{z}$. The RBC system is controlled by two dimensionless parameters, i.e. the Rayleigh number $Ra = \alpha g \Delta T H^3/(\nu\kappa)$ and the Prandtl number $Pr = \nu/\kappa$. Here α, ν and κ are the thermal expansion coefficient, the kinematic viscosity and the thermal diffusivity of the working fluid, respectively. The applied temperature difference and the gravitational acceleration constant are denoted as ΔT and g, respectively. Studying the regime with strong spatial confinement, characterized by the aspect ratio $\Gamma = D/H < 1$ (D is the cell diameter) is of particular importance because, from the definition of Ra, one recognizes that $Ra \propto H^3$. It thus becomes relatively easy to achieve high Ra with $\Gamma < 1$ for a cell with fixed D. However, compared with many studies in the $\Gamma \geq 1$ regime (see, for example, Funfschilling *et al.* 2005; Bailon-Cuba, Emran & Schumacher 2010; Van Der Poel, Stevens & Lohse 2011; Wang *et al.* 2020), the effects of the spatial confinement on the flow-state evolution in liquid-metal convection remain obscure.

For the onset of convection, recent theories show that the onset Rayleigh number $Ra_c \sim \Gamma^{-4}$ in the limit of $\Gamma \ll 1$ (Chandrasekhar 1961; Shishkina 2021; Ahlers *et al.* 2022; Zhang & Xia 2023). For a cell with $\Gamma = 1/10$, similarities between the fluctuations of velocity and temperature statistics are found when compared to a cell with $\Gamma = 25$ (Pandey *et al.* 2022). In turbulent liquid-metal convection with $\Gamma = 1/2$, the collapse of the large-scale circulation was reported (Schindler *et al.* 2022) and a strong coupling between the internal flow structure and heat transport efficiency was found (Chen *et al.* 2023). As Ra increases, the liquid-metal convection exhibits rich dynamics, i.e. the flow evolves from conduction to convection, oscillation, chaos and turbulence (Verzicco & Camussi 1997; Ren *et al.* 2022). How the flow-state transitions, especially the onset of

convection and the transition to fully developed turbulence, will be altered in the strongly confined regime motivates the present experimental and numerical study.

We will show that with increasing spatial confinement, the flow-state evolution mentioned above remains. The transitional Ra between different flow states is postponed due to the stabilization effect in the strongly confined cells. However, the transition to the fully developed turbulent state is accelerated in cells with $\Gamma \ll 1$ if the flow state is characterized by a supercritical Rayleigh number Ra/Ra_c. For example, while the flow becomes fully developed turbulence at $Ra \approx 200Ra_c$ in a $\Gamma = 1$ cell, the same transition in a $\Gamma = 1/20$ cell only requires $Ra \approx 3Ra_c$. Using direct numerical simulation (DNS) and linear stability analysis (LSA), we will show that when $\Gamma \ll 1$, the system develops multiple vertically aligned rolls just above the onset of convection, allowing more vertical high-wavenumber modes to develop with decreasing Γ. The frequent transitions between different vertical flow modes when Ra is increased results in the flow becoming turbulent in a much earlier stage when $\Gamma \ll 1$.

2. The experimental and numerical set-ups

The experiment was carried out in cylindrical RBC cells with liquid-metal alloy gallium-indium-tin (GaInSn) as the working fluid. The physical properties of GaInSn are documented in Ren *et al.* (2022). Its Prandtl number is $Pr = 0.029$ at a mean fluid temperature of 35 °C. To cover a large Ra range, two sets of convection cells with diameters of $D = 20.14$ mm and $D = 40.37$ mm were constructed. They are referred to as set A and set B hereafter. For set A, the aspect ratio of the cells vary in the range of $1/20 \leq \Gamma \leq 1$. For set B, the aspect ratio changes in the range of $1/3 \leq \Gamma \leq 1$. The details on the cell diameter D and height H can be found in table 2 in the Appendix. In addition, table 2 lists some parameters of the experiment, such as the range of ΔT, applied heat flux at the bottom plate q and the range of Biot number Bi.

In total eight convection cells were constructed. They were identical in design. The detailed construction of the convection cell and experimental procedure can be found in Ren *et al.* (2022). We mention here the essential features of a cell from set A with $\Gamma = 1$. It consists of a top copper cooling plate, a bottom copper heating plate, and a Plexiglas sidewall. The top plate with a diameter of 20.14 mm was cooled by circulating temperature-regulated cooling water. The temperature stability of the cooling water is better than 0.01 K (Julabo, Dyneo DD-1000). The bottom plate was heated with a wire heater embedded in grooves on its backside. The heater was connected to a power supply with a long-term stability of 99.99 % (Ametex, XG 1500). The sidewall with a height of $H = 20.03$ mm was made of Plexiglas. Its thermal conductivity is 0.192 W $(\mathrm{mK})^{-1}$.

Temperatures of the top (bottom) plate were measured using 3 (4) thermistors (Omega, 44031), from which Ra and Pr were calculated. The thermistor heads were located at a distance of 3 mm from the fluid–plate contact surface. The heat flux q supplied at the bottom plates was calculated using the measured current I and voltage V supplied to the heater with a four-wire method, i.e. $q = 4VI/(\pi D^2)$. The Nusselt number, which quantifies the ratio between the heat flux transported by the system and that by conduction alone, is calculated using $Nu = qH/(\lambda \Delta T)$ with $\lambda = 24.9$ W $(\mathrm{mK})^{-1}$ being the thermal conductivity of GaInSn. The resistances of the thermistors and the voltage supplied to the heater were measured using a digital multimeter (Keysight, 34972A) at a sampling rate of 0.35 Hz. The heat leakage was minimized by adding temperature-controlled side and bottom thermal shields to the cell. The convection cells were levelled better than 0.029°. The temperature boundary condition at the sidewall is approximately adiabatic. The time-averaged spatial temperature homogeneity as measured by 4 (3) embedded

thermistors in the bottom (top) plate is within 3 % of ΔT. The root-mean-square (r.m.s.) temperatures of the top and bottom plates are within 2 % of ΔT for most of the cells. Two exceptions are the set B cells with $\Gamma = 1/2$ and 1/3. It is observed that the r.m.s. temperature of the bottom plate in these two cells reaches 6 % and 4 % of ΔT. A thermistor with a head diameter of 0.38 mm and a time constant of 30 ms in liquid (Measurement Specialties, GAG22K7MCD419) was placed at the cell centre to probe the temperature fluctuation. In addition, a multi-thermal probe method (Xie, Wei & Xia 2013) was used to measure the large-scale flow (LSF) structures inside the convection cell. This method could measure the structure and dynamics of LSF in liquid-metal convection accurately (Zürner *et al.* 2019; Ren *et al.* 2022). Combining the measurements of the temperature fluctuation at the cell centre and the LSF structure and dynamics, the flow states in the five cells with different Γ can be determined. We refer to Ren *et al.* (2022) for more details on determining the flow states.

Complementary DNS of the governing Oberbeck–Boussinesq equations was carried out using the CUPS code in the $1/50 \leq \Gamma \leq 1$ range. The simulation was conducted in cylindrical domains with no-slip velocity boundary conditions at all walls, adiabatic temperature conditions at the sidewall, and isothermal boundary conditions at the top and bottom plates. For details on the CUPS code and its verification, we refer to Chong, Ding & Xia (2018). The Ra_c was evaluated from the DNS data. The flow structure at $Ra = 3Ra_c$ (note Ra_c depends on Γ) was simulated to illustrate how spatial confinement alters the flow structures. In addition, LSA was carried out to determine the stability curve of different vertical flow modes.

3. Results and discussions

3.1. *The critical Rayleigh number Ra_c for the onset of convection vs Γ*

In this section, we study how confinement affects the onset of convection. Note that Ra_c is independent of Pr from LSA (Chandrasekhar 1961). Figure 1(a) plots the measured $Nu - 1$ as a function of Ra together with the scaled time-averaged amplitude $\delta/\Delta T$ of the first Fourier mode measured from the azimuthal temperature profile at the midheight of a $\Gamma = 1$ cell. We have $Nu - 1 = 0$ and $\delta/\Delta T = 0$ in the conduction state. The measured δ aligns with the smallest temperature difference we can resolve experimentally (the dashed line in the figure). However, due to unknown parasitic heat leakage, the Nu measured in the conduction state is slightly above 1. Combining Nu and δ measurements, we conclude that the system starts from the conduction state at $Ra \sim 4000$ and evolves into the convection state with increasing Ra. The inset shows the streamlines of the flow field obtained at $Ra \approx Ra_c$ numerically in a $\Gamma = 1$ cell with red and blue colours representing ascending and descending flow, respectively. The LSF is a single-roll structure, consistent with the observation that the first Fourier mode is the dominant mode obtained from the sidewall temperature profiles.

It was predicted theoretically that the Nu just above the onset of convection depends linearly on Ra (Malkus & Veronis 1958). Thus, by fitting the Nu data deviated from the horizontal dashed line (the conduction state) and finding the intersection point between the extrapolation of this linear fitting function with the horizontal dashed line, we determine $Ra_c = 5170$ from Nu measurement. Figure 1(a) also shows that $\delta/\Delta T$ increases linearly with Ra just above onset. Similar to $Nu - 1$, we can also determine Ra_c from $\delta/\Delta T$ by the linear fitting method, which yields $Ra_c = 5095$. The two values of Ra_c agree with each other within 2 %.

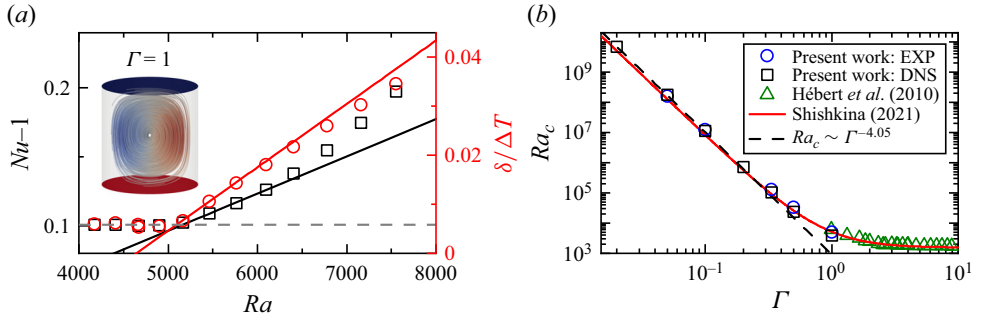

Figure 1. (*a*) Determination of the critical Rayleigh number Ra_c for the onset of convection in a $\Gamma = 1$ cell based on Nu (squares) and the amplitude $\delta/\Delta T$ of the LSF (circles) obtained from experiment. (*b*) The Ra_c vs Γ from present experiment and DNS. The dashed line marks $Ra_c \sim \Gamma^{-4.05}$ fitted to the data with $\Gamma \leq 1/10$. The solid line is a theoretical prediction from Shishkina (2021). The triangles are Ra_c measured in the $\Gamma \geq 1$ regime with $Pr = 28.9$ from Hébert *et al.* (2010).

The above analysis of Nu measured experimentally in the range of $1/20 \leq \Gamma \leq 1/2$ and that obtained numerically for $1/50 \leq \Gamma \leq 1$ were repeated. The so-determined Ra_c as a function of Γ is plotted in figure 1(*b*). The experimentally determined Ra_c agrees with the numerically obtained Ra_c. Similar to the observation by Zhang & Xia (2023) and Müller, Neumann & Weber (1984), with decreasing Γ, Ra_c shows a rapid increase. For comparison, we also plot in the figure Ra_c measured experimentally for $\Gamma \geq 1$ in a working fluid with $Pr = 28.9$ from Hébert *et al.* (2010) and the theoretical prediction of $Ra_{c,\Gamma} = (2\pi)^4(1 + (1.4876/\Gamma^2))(1 + (0.3435/\Gamma^2))$ from Shishkina (2021) with adiabatic sidewall temperature boundary conditions. Figure 1(*b*) shows the experimental data, numerical data and theoretical prediction agree excellently with each other over almost three decades in Γ. The results also imply the sidewall boundary condition of the experiment can be treated as adiabatic to a good approximation. In addition, when $\Gamma \leq 1/10$, the data can be fitted by $Ra_c = 915\Gamma^{-4.05}$ (the dashed line).

3.2. *Flow-state evolution in spatially confined cells ($\Gamma < 1$)*

We now study the flow-state evolutions when Ra increases beyond Ra_c. Previous studies in liquid-metal convection with $\Gamma = 1$ show that the flow evolves from the convection state to an oscillation state, a chaotic state, a transition-to-turbulence state and a fully developed turbulent state (Verzicco & Camussi 1997; Ren *et al.* 2022). The different flow states exhibit different natures of the temperature fluctuations at the cell centre. For the convection state, there is hardly any temperature fluctuation. The scaled r.m.s. temperature at the cell centre $\sigma_{T_c}/\Delta T$ increases beyond zero when the system becomes time-dependent, i.e. in the oscillation state. In the chaotic state and the transition-to-turbulence state, $\sigma_{T_c}/\Delta T$ increases with Ra. But these two states are characterized by different scaling relations between $\sigma_{T_c}/\Delta T$ and Ra. The $\sigma_{T_c}/\Delta T$ reaches maximum at the boundary between the transition-to-turbulence state and the fully developed turbulence state. When the system becomes fully developed, one observes a negative scaling law between $\sigma_{T_c}/\Delta T$ and Ra that is widely observed in working fluid like water (see, for example, Xie *et al.* 2019). Thus, the transitional value of Ra between different states can be determined based on the temperature fluctuation measured at the cell centre.

Figures 2(*a*)–2(*d*) plot the scaled temperature fluctuation in cells with $\Gamma = 1/2$, 1/3, 1/10 and 1/20, respectively. Following Ren *et al.* (2022), the temperature fluctuations

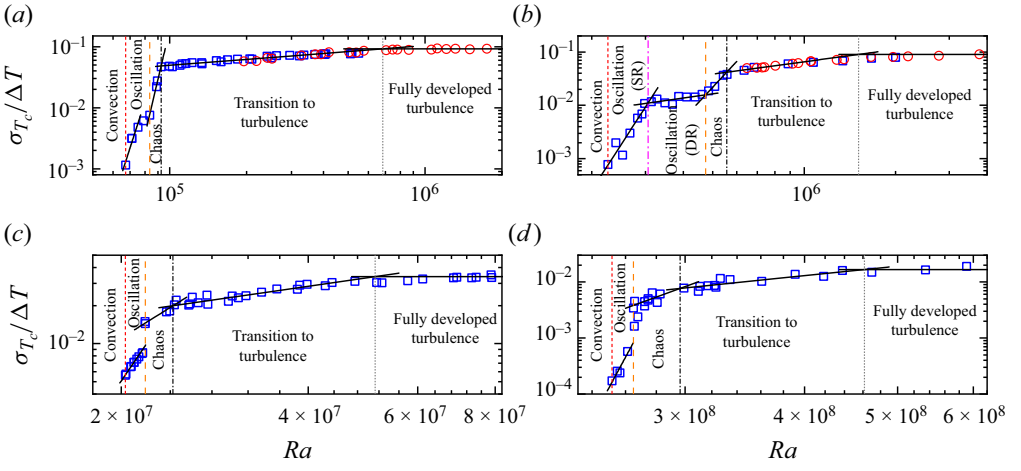

Figure 2. Determination of the flow state based on the experimentally measured scaled temperature fluctuations at the cell centre $\sigma_{T_c}/\Delta T$ as a function of Ra in cells with (*a*) $\Gamma = 1/2$; (*b*) $\Gamma = 1/3$; (*c*) $\Gamma = 1/10$ and (*d*) $\Gamma = 1/20$. The blue squares represent data measured in the set A cells and the red circles in (*a*,*b*) are data measured in the set B cells. In (*b*) the SR and DR refer to single-roll and double-roll, respectively.

for different states are fitted by respective power laws. The transitional Rayleigh numbers between different states are then determined when two power laws cross. The so-determined flow states are labelled in figure 2. Note the flow-state transition can also be determined from the dynamics of the LSF, i.e. its flow strength δ, azimuthal orientation θ, and their respective fluctuations. The boundaries between different flow states show no noticeable qualitative difference based on either the temperature fluctuation method or the dynamics of the LSF.

To study systematically the effects of Γ on flow-state evolution, we plot the flow state in a two-dimensional phase space composed of either $\Gamma - Ra$ or $\Gamma - (Ra/Ra_c)$. The results are plotted in figures 3(*a*) and 3(*b*), respectively. Note in figure 3(*b*), Ra for each Γ is normalized by its own Ra_c. We first examine the flow-state evolution in the $\Gamma - Ra$ plot. One sees that the flow in cells with $1/20 \leq \Gamma \leq 1$ all exhibit a conduction state, a convection state, an oscillation state, a chaotic state, a transition-to-turbulence state and a fully developed turbulent state. However, with decreasing Γ, significant changes in the flow-state transition can be observed. Not only Ra_c is postponed to larger values as discussed in § 3.1. The transitional values of the other flow states are all postponed to larger Ra due to the stabilization effect caused by spatial confinement. The transitional Rayleigh number to the fully developed turbulent state, defined as Ra_f here (see purple left-pointing triangles in figure 3*a*) can be fitted by a power law with Γ for $\Gamma \leq 1/3$, i.e. $Ra_f = 5.40 \times 10^4 \Gamma^{-3.01}$. The results suggest that the damping effect on the transition to the fully developed turbulent state by the stabilization effects of the wall when decreasing Γ becomes weak when compared with that on the onset of convection, which is $Ra_c \sim \Gamma^{-4.05}$. It should be noted that the $Ra_f \sim \Gamma^{-3.01}$ scaling is only valid in the studied parameter range, i.e, $1/20 \leq \Gamma \leq 1/3$. In addition, we note if the observed scaling is valid for $\Gamma \ll 1$, one obtains $Ra_f/Ra_c \sim \Gamma^{-3.01}/\Gamma^{-4.05} \sim \Gamma$. However, since the Γ is not asymptotically small and the range of Γ in the present study is limited, one sees that $Ra_f/Ra_c \sim \Gamma^{1.33}$ to the first order as shown in figure 3(*b*). It will be very interesting to study what will happen when Γ becomes even smaller than the present study.

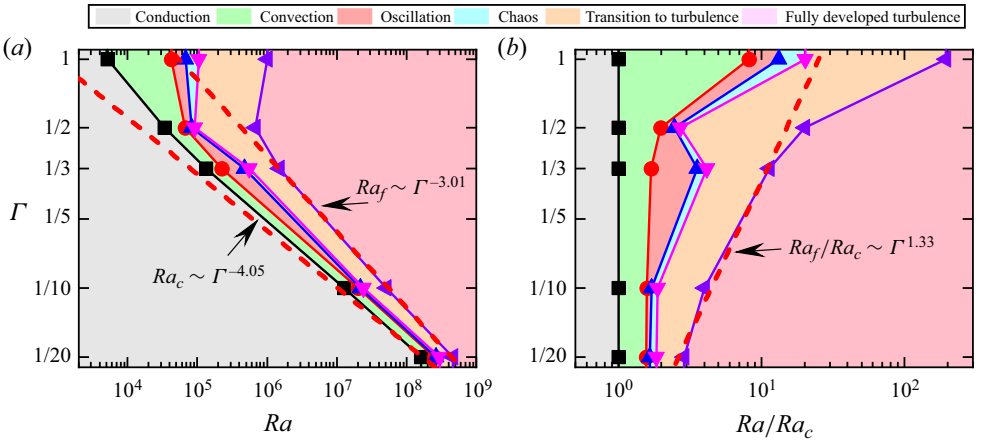

Figure 3. (*a*) Experimentally obtained flow-state evolution in the $\Gamma - Ra$ phase space. The flow states are marked by different colours indicated in the legend. The symbols are experimentally determined transitional Rayleigh numbers between different flow states. The solid lines are used to guide the eye. The lower dashed line marks the onset Rayleigh number $Ra_c = 915\Gamma^{-4.05}$ and the upper dashed line marks the transition to fully developed turbulence Rayleigh number $Ra_f = 5.40 \times 10^4\Gamma^{-3.01}$. (*b*) The phase diagram plotted in the $\Gamma - (Ra/Ra_c)$ phase space. The dashed line is a fitting of $Ra_f/Ra_c \sim \Gamma^{1.33}$.

Although we do not have a theoretical understanding of this $\Gamma^{-3.01}$ dependence, we note a similar Γ^{-3} dependence for the transition to the ultimate state in turbulent RBC with gas as the working fluid was reported (Roche *et al.* 2010; Ahlers *et al.* 2022; He, Bodenschatz & Ahlers 2022). As we will show later, the transition to the fully developed turbulent state is characterized by the loss of spatial coherence of the LSF. In contrast, the transition to the ultimate regime results from the boundary layer becoming turbulent (Kraichnan 1962). Thus, the two Γ^{-3} scalings may originate from different flow physics.

Now let us discuss the flow-state evolution in the $\Gamma - (Ra/Ra_c)$ plot shown in figure 3(*b*), which is usually employed when studying flow-state transitions in the vicinity of onset. When Γ is changed from 1 to 1/2, one sees that all the transitions are advanced, occurring at smaller values of Ra/Ra_c. The initiation of the oscillation instability occurs at $Ra/Ra_c \approx 1.6$, and it is almost independent of Γ for $1/20 \leq \Gamma \leq 1/3$. For $1/20 \leq \Gamma \leq 1/10$, the transition from the oscillation state to the chaotic state and that from the chaotic state to the transition-to-turbulence state occur at $Ra/Ra_c = 1.68$ and $Ra/Ra_c = 1.86$, respectively. Both seem to be independent of Γ. The enlarged portion of the oscillation state and the consequent delay of the chaotic state in the cell with $\Gamma = 1/3$ originates from a bifurcation of the flow from a single-roll (SR) structure to a double-roll (DR) structure, which we will discuss in detail elsewhere (authors' unpublished observations). Figure 3(*b*) also reveals that the transition to fully developed turbulence occurs at a much earlier stage for smaller Γ, e.g. the flow in the $\Gamma = 1$ cell becomes fully developed turbulence at $Ra \approx 200Ra_c$. It occurs at $Ra \approx 3Ra_c$ in the cell with $\Gamma = 1/20$. The observation suggests that despite delaying the onset of convection due to the stabilization effects caused by strong spatial confinement, it advanced the transition to turbulence. Thus, slender geometries could be utilized to achieve fully developed turbulence in a relatively accessible way by reducing the cell diameter.

Recently, Zhang & Xia (2023) studied heat transport in slender cuboid RBC using water as the working fluid with the $Pr = 4.38$. They classified the flow states in their quasi-one-dimensional cells based on the heat transport behaviour of the

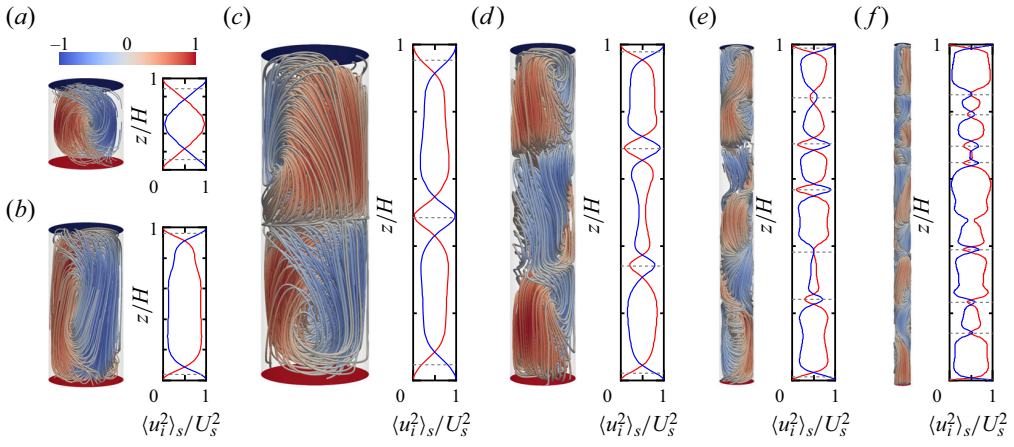

Figure 4. Numerically obtained instantaneous flow structure at $Ra/Ra_c = 3$ for (*a*) $\Gamma = 1$ with number of rolls being $n = 1$; (*b*) $\Gamma = 1/2$, $n = 1$; (*c*) $\Gamma = 1/3$, $n = 2$; (*d*) $\Gamma = 1/5$, $n = 3$; (*e*) $\Gamma = 1/10$, $n = 6$; and (*f*) $\Gamma = 1/20$, $n = 8$. For each panel, the left subplot shows the streamlines with red and blue colours representing ascending and descending flow, respectively. The right subplot shows the vertical profiles of the horizontally averaged normalized squared horizontal velocity $E_h(z) = \sum_{i=x,y}\langle u_i^2(z)\rangle_S/U_S^2(z)$ (blue line) and the squared vertical velocity $E_v(z) = \langle u_z^2(z)\rangle_S/U_S^2(z)$ (red line). Here $\langle\cdots\rangle_S$ means averaging over a horizontal cross-section and $U_S^2(z) = \sum_{i=x,y,z}\langle u_i^2(z)\rangle_S$ is the total energy at a certain z. The horizontal dashed lines mark the boundary between adjacent rolls.

system, i.e. a viscous-dominated regime, a plume-controlled regime and a classical boundary-layer-controlled regime. The present study differs from Zhang & Xia (2023) in two ways: firstly, we are working with Pr which is two orders of magnitude smaller than that reported in Zhang & Xia (2023); secondly, the phase diagram shown in figure 3 is not based on the heat transport, but based on the structure and dynamics of the flow.

3.3. *Dynamics of the LSF with decreasing* Γ

To reveal the mechanism that accelerates the transition to turbulence in strongly confined cells, we study the structure and dynamics of the LSF. Figures 4(*a*)–4(*f*) show the instantaneous flow structure numerically obtained at $Ra/Ra_c = 3$ in cells with $1/20 \leq \Gamma \leq 1$. Supplementary movies are available at https://doi.org/10.1017/jfm.2024.86 showing the temporal evolution of the flow structure. While the flow is in the convection state for $\Gamma = 1$, the oscillation state for $\Gamma = 1/2$ and 1/3, the chaotic state for $\Gamma = 1/5$, it is in the turbulent state for $\Gamma \leq 1/10$. Following Zwirner, Tilgner & Shishkina (2020), we use the relation between the horizontally averaged squared horizontal velocity $E_h = \sum_{i=x,y}\langle u_i^2\rangle_S/U_S^2$ and the squared vertical velocity $E_v = \langle u_z^2\rangle_S/U_S^2$ to identify the flow structures. Here $\langle\cdots\rangle_S$ means averaging over a horizontal cross-section and $U_S^2 = \sum_{i=x,y,z}\langle u_i^2\rangle_S$ is the total energy at a certain horizontal cross-section. The left subplot of each panel in figure 4 shows the streamlines with red and blue colours representing ascending and descending flow, respectively. The right subplot of each panel shows the vertical profiles of E_h (blue line) and E_v (red line). For a continuous vertical roll to exist, we require $E_v(z) > E_h(z)$. To determine the junction between two neighbouring rolls, we first find two neighbouring $E_v(z) = E_h(z)$ points. The midpoint of these two neighbouring points with $E_h(z) > E_v(z)$ is then defined as the junction between two rolls (see the dashed line in the right subplots of each panel in figure 4). From figure 4(*a*,*b*), one sees that for

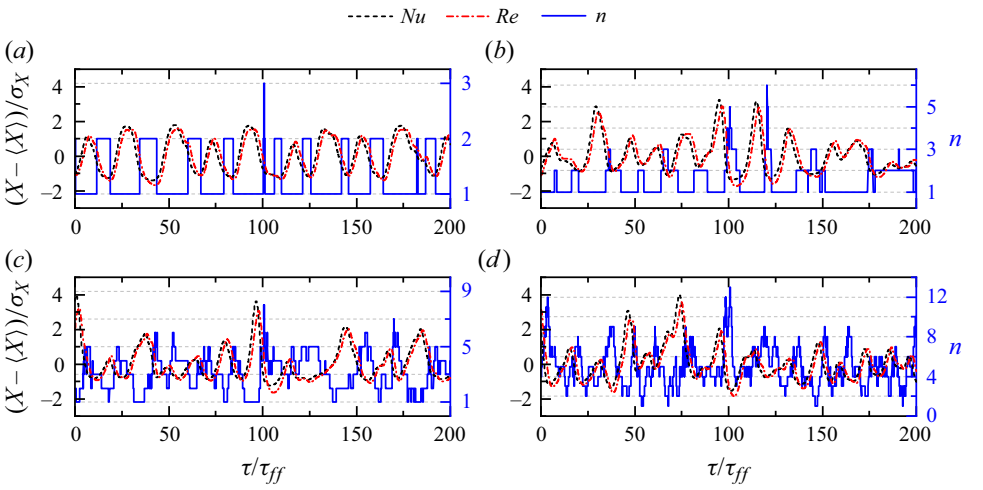

Figure 5. Time series of the number of rolls n (blue solid line), the Nusselt number Nu (black dashed line) and the Reynolds number Re (red dash-dotted line) in cells with (*a*) $\Gamma = 1/3$; (*b*) $\Gamma = 1/5$; (*c*) $\Gamma = 1/10$; and (*d*) $\Gamma = 1/20$ obtained numerically at $Ra/Ra_c = 3$. In the vertical axis title, X represents either Nu, Re or n, and σ_X represents their respective r.m.s. value.

	$\Gamma = 1/2$			$\Gamma = 1/3$			$\Gamma = 1/5$			$\Gamma = 1/10$			$\Gamma = 1/20$		
n	τ	P%	Nu	τ	P%	Nu	τ	P%	Nu	τ	P%	Nu	τ	P%	Nu
1	248.58	99.6	1.53	14.61	72.9	1.80	6.93	51.0	2.03	1.85	13.9	2.21	0.75	0.8	2.27
2	1.06	0.4	1.27	5.21	26.8	1.27	2.44	33.5	1.47	1.36	27.7	1.90	0.66	5.1	2.30
3	—	—	—	0.59	0.1	1.19	1.88	14.2	1.31	1.13	28.5	1.73	0.63	13.3	2.12
4	—	—	—	—	—	—	0.34	0.5	1.33	0.88	18.1	1.57	0.55	19.9	1.98
5	—	—	—	—	—	—	—	—	—	0.71	7.9	1.47	0.45	20.0	1.89
6	—	—	—	—	—	—	—	—	—	0.41	1.5	1.39	0.38	15.7	1.79
7	—	—	—	—	—	—	—	—	—	0.33	0.3	1.30	0.36	11.2	1.70
8	—	—	—	—	—	—	—	—	—	—	—	—	0.30	5.8	1.65
9	—	—	—	—	—	—	—	—	—	—	—	—	0.26	2.3	1.62
10	—	—	—	—	—	—	—	—	—	—	—	—	0.18	0.6	1.56
11	—	—	—	—	—	—	—	—	—	—	—	—	0.26	0.3	1.52

Table 1. The mean lifetime τ in units of free-fall time τ_{ff}, the probabilities of occurrence P and the mean heat transport efficiency Nu of the n-roll flow mode for $Ra/Ra_c = 3$ at $Pr = 0.029$. The symbol '—' means no such flow modes are observed in the study. Each simulation runs at least 1800 τ_{ff} after the system has reached a steady state.

$\Gamma = 1$ and 1/2, the LSF is in the form of a single-roll structure similar to the onset of convection (inset of figure 1*a*). This is also verified by the observation that $E_v > E_h$ for the entire cell except for the locations very close to the top and bottom boundaries where large parts of the flow in the boundary layers are in the horizontal directions, resulting in $E_h > E_v$. When $\Gamma \leq 1/3$, the flow structure becomes complex: a double-roll structure in the $\Gamma = 1/3$ cell and a triple-roll structure in the $\Gamma = 1/5$ cell. There are eight vertically stacked rolls for the extreme case with $\Gamma = 1/20$.

To study systematically the temporal evolution of the flow structure, we show in figure 5 the time trace of the number of rolls n, the corresponding Nu and Re. Table 1 summarizes the statistics of different flow modes in cells with $1/20 \leq \Gamma \leq 1/2$, including their mean

lifetime τ, the probability of occurrence P and the corresponding Nu. The symbol '—' means no such flow mode is observed during the simulation, which runs at least 1800 τ_{ff}. In the $\Gamma = 1$ cell (not shown), the structure of the LSF is a stable single roll similar to the instantaneous examples shown in figure 4(*a*). When decreasing Γ, one sees that, firstly, the maximum number of rolls the system can develop n_{max} increases significantly from $n_{max} = 1$ for $\Gamma = 1$ to $n_{max} = 11$ for $\Gamma = 1/20$. Secondly, the system switches more frequently between flow mode with different n for smaller Γ, e.g. for the $\Gamma = 1/3$ cell, the system switches almost periodically between the $n = 1$ and $n = 2$ modes; it switches frequently and chaotically between flow modes from $n = 1$ to $n = 13$ in the $\Gamma = 1/20$ cell. As a result of the increased number of rolls and frequent switching among them, the average lifetime of each mode decreases dramatically with decreasing Γ. For example, in the $\Gamma = 1/3$ cell, the mean lifetime τ for the $n = 1$ and the $n = 2$ modes are $\tau_1 = 14.61\tau_{ff}$ and $\tau_2 = 5.21\tau_{ff}$, respectively. In contrast, in the $\Gamma = 1/20$ cell, due to the frequent transitions between modes with different n, the mean lifetime of each mode is less than τ_{ff}. The maximum lifetime observed is $\tau_1 = 0.75\tau_{ff}$ and the minimum mean lifetime observed is $\tau_{10} = 0.18\tau_{ff}$. These observations suggest that in the strongly confined cells, the single-roll large-scale circulation observed in systems with $\Gamma \sim 1$ collapses. As a result of this new dynamical process of flow-mode transition discussed above that exists only in confined geometries, the flow becomes turbulent very quickly after the onset of convection.

The change in the flow state with Γ is also reflected on the Nu and Re time series shown in figure 5. One sees that both Nu and Re oscillate periodically in the cell with $\Gamma = 1/3$. With decreasing Γ, the fluctuation of Nu and Re increases. They reach up to four times the r.m.s. value in the $\Gamma = 1/20$ cell. Consistent with the finding by Zwirner *et al.* (2020), for a given Γ, the higher the number of vertical rolls, the smaller the heat transport efficiency of the system. For example, in the cell with $\Gamma = 1/20$, the maximum Nu observed for $n = 1$ mode is 50 % higher than Nu of the $n = 11$ mode. It should also be noted that there is a negative time delay between n and Nu or Re, suggesting that the flow-mode change is probably the cause for the variation in Nu and Re.

Finally, let us try to understand the origin of the multiple vertically stacked rolls based on LSA. We consider an RBC cell with no-slip and constant temperature boundary conditions at the top and bottom walls. The two horizontal directions are periodic. The height of the cell H is fixed to be 1. Thus, its aspect ratio is $\Gamma = D/H = D$. Limiting the discussion with only one cell in the horizontal direction requires $k_x D = \pi$. Following the standard LSA procedure (Chandrasekhar 1961), we obtain the marginal stability curve for the cell with the horizontal wavenumber $k^2 = k_x^2 + k_y^2 = 2k_x^2$ and different numbers of vertically stacked rolls n. Here k_x and k_y are the two horizontal wavenumbers. Next we replace k from the LSA analysis with Γ using the relation $\Gamma = \pi/k_x = \pi/k_y = \sqrt{2}\pi/k$. Figure 6(*a*) plots the marginal stability curve from $n = 1$ to $n = 10$ vertically stacked rolls in the $Ra - \Gamma$ diagram. Firstly, it is seen that the marginal stability curves for different modes do not cross each other with decreasing Γ. Secondly, the curves for the $n > 1$ modes gradually approach the limit of $Ra_{c,n=1} = 390\Gamma^{-4}$ (the dashed line) for $\Gamma \ll 1$, suggesting that in the strongly confined regime, the high-order modes become unstable just above the onset of convection. This can be seen more clearly from figure 6(*b*), where the marginal stability curves for the $n > 1$ modes are normalized by that of the $n = 1$ mode. The figure suggests that for $Ra = 3Ra_c$ and $\Gamma < 1/10$, all modes up to $n = 9$ will grow, consistent with the DNS observation.

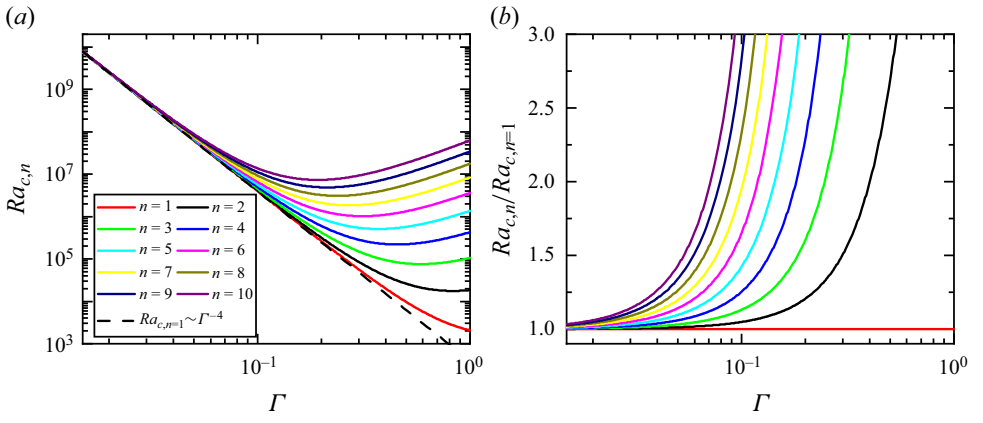

Figure 6. (*a*) Marginal stability curve for different numbers of vertically aligned rolls n vs the aspect ratio Γ. The dashed line marks $Ra_c \sim \Gamma^{-4}$ for the $n = 1$ mode. (*b*) The marginal stability curve of the $n > 1$ modes normalized by that of the $n = 1$ mode as a function of Γ.

4. Conclusion

We have systematically studied the flow-state evolution in liquid-metal convection in a strongly confined regime. Combining experiment, DNS and LSA, we show that not only the onset of Rayleigh–Bénard instability is delayed due to the stabilizing effect in strongly confined geometries, but the various flow-state transitions are all postponed. The onset Rayleigh number Ra_c and the transition to fully developed turbulence Rayleigh number Ra_f depend on the aspect ratio Γ with $Ra_c \sim \Gamma^{-4.05}$ for $\Gamma \leq 1/10$ and $Ra_f \sim \Gamma^{-3.01}$ for $\Gamma \leq 1/3$, implying that the stabilization effects are weaker on the transition to fully developed turbulence when compared with that on the onset. The study shows that spatial confinement facilitates the transition to turbulence if the flow-state transition is expressed in terms of a supercritical Rayleigh number, i.e. Ra/Ra_c. The reason for this can be attributed to a new mechanism for transition to turbulence in the strongly confined limit. The LSA shows high-order vertical flow modes appear just above the onset of convection in strong spatially confined cells. With increasing Ra, the system stochastically switches between different vertical flow modes. As a result of this frequent flow-mode switching, the usually observed single-roll structure in the $\Gamma \sim 1$ regime breaks down, and the system becomes fully developed turbulence in an early stage. Turbulence with stabilization forces is common in nature and industry, such as rotation and magnetic fields in geophysical and astrophysical applications. The newly discovered mechanism for transition to fully developed turbulence may find applications in other turbulent flows.

Supplementary movies. Supplementary movies showing the temporal evolution of the large-scale flow structure in different Γ cells are available at https://doi.org/10.1017/jfm.2024.86.

Acknowledgements. We are grateful to R. Kerswell for pointing us to the analysis of the problem using LSA. We also thank C. Sun, S.-D. Huang and L. Zhang for discussions.

Funding. This work was supported by the NSFC grant nos 92152104, 12232010, 12072144 and a XJTU Young Talent Support Plan.

Declaration of interests. The authors report no conflict of interest.

Author ORCIDs.
Lei Ren https://orcid.org/0000-0001-8256-0834;
Xin Tao https://orcid.org/0000-0002-7070-0788;

Ke-Qing Xia https://orcid.org/0000-0001-5093-9014;
Yi-Chao Xie https://orcid.org/0000-0002-2159-4579.

Author contributions. L.R. and X.T. contributed equally to this work.

Appendix

Table 2 lists some of the parameters of the convection cells and of the experiment in the present study. In total, eight convection cells were used. In the table, the cell diameter D, height H, the aspect ratio Γ, the range of temperature difference between the top and bottom plate ΔT, the range of the heat flux q supplied at the bottom plate and the Biot number Bi are listed.

Cell	D (mm)	H (mm)	Γ (nominal Γ)	ΔT (K)	Heat flux q (W cm^{-2})	Biot number
A	20.14	20.03	1.01 (1)	1.82∼11.40	0.26∼3.30	0.051∼0.134
		39.88	0.50 (1/2)	1.47∼24.15	0.11∼5.81	0.026∼0.111
		59.84	0.34 (1/3)	1.62∼26.05	0.08∼4.65	0.018∼0.083
		200.15	0.10 (1/10)	4.50∼30.71	0.07∼1.51	0.006∼0.023
		399.9	0.05 (1/20)	6.88∼29.92	0.07∼0.61	0.003∼0.009
B	40.37	40.04	1.01 (1)	0.51∼26.91	0.05∼8.67	0.034∼0.152
		80.05	0.50 (1/2)	0.48∼26.70	0.03∼6.67	0.020∼0.119
		119.83	0.34 (1/3)	0.50∼22.28	0.02∼4.41	0.011∼0.094

Table 2. Some parameters of the convection cells and of the experiment. Here $\Gamma = D/H$ is the aspect ratio of the cell with D and H being the cell diameter and height, respectively. The nominal Γ is used to refer to each cell in the main text; $\Delta T = T_{bot} - T_{top}$ denotes the time-averaged temperature difference between the bottom plate T_{bot} and the top plate T_{top}. The heat flux supplied at the bottom plate is listed as q. The range of the Biot number, defined as $Bi = Nu(\lambda/\lambda_{Cu})(H_{Cu}/H))$, is shown in the last column for each cell with $\lambda_{Cu} = 401$ W (mK)$^{-1}$ and $H_{Cu} = 19$ mm for the bottom plate and 15 mm for the top plate.

References

Ahlers, G., *et al.* 2022 Aspect ratio dependence of heat transfer in a cylindrical Rayleigh–Bénard cell. *Phys. Rev. Lett.* **128**, 084501.

Ahlers, G., Grossmann, S. & Lohse, D. 2009 Heat transfer and large scale dynamics in turbulent Rayleigh–Bénard convection. *Rev. Mod. Phys.* **81**, 503–537.

Bailon-Cuba, J., Emran, M.S. & Schumacher, J. 2010 Aspect ratio dependence of heat transfer and large-scale flow in turbulent convection. *J. Fluid Mech.* **655**, 152–173.

Chandrasekhar, S. 1961 *Hydrodynamic and Hydromagnetic Stability*. Oxford University Press.

Chen, X.-Y., Xie, Y.-C., Yang, J.-C. & Ni, M.-J. 2023 Strong coupling of flow structure and heat transport in liquid metal thermal convection. *J. Fluid Mech.* **975**, A21.

Chillá, F. & Schumacher, J. 2012 New perspectives in turbulent Rayleigh–Bénard convection. *Eur. Phys. J.* E **35**, 58.

Chong, K.L., Ding, G. & Xia, K.-Q. 2018 Multiple-resolution scheme in finite-volume code for active or passive scalar turbulence. *J. Comput. Phys.* **375**, 1045–1058.

Chong, K.L., Yang, Y., Huang, S.-D., Zhong, J.-Q., Stevens, R.J.A.M., Verzicco, R., Lohse, D. & Xia, K.-Q. 2017 Confined Rayleigh–Bénard, rotating Rayleigh–Bénard, and double diffusive convection: a unifying view on turbulent transport enhancement through coherent structure manipulation. *Phys. Rev. Lett.* **119**, 064501.

Funfschilling, D., Brown, E., Nikolaenko, A. & Ahlers, G. 2005 Heat transport by turbulent Rayleigh–Bénard convection in cylindrical samples with aspect ratio one and larger. *J. Fluid Mech.* **536**, 145–154.

GLATZMAIER, G.A., COE, R.S., HONGRE, L. & ROBERTS, P.H. 1999 The role of the Earth's mantle in controlling the frequency of geomagnetic reversals. *Nature* **401**, 885–890.

HE, X., BODENSCHATZ, E. & AHLERS, G. 2022 Universal scaling of temperature variance in Rayleigh–Bénard convection near the transition to the ultimate state. *J. Fluid Mech.* **931**, A7.

HÉBERT, F., HUFSCHMID, R., SCHEEL, J. & AHLERS, G. 2010 Onset of Rayleigh–Bénard convection in cylindrical containers. *Phys. Rev.* E **81**, 046318.

HUANG, S.-D., KACZOROWSKI, M., NI, R. & XIA, K.-Q. 2013 Confinement-induced heat-transport enhancement in turbulent thermal convection. *Phys. Rev. Lett.* **111**, 104501.

KRAICHNAN, R.H. 1962 Turbulent thermal convection at arbitrary Prandtl number. *Phys. Fluids* **5**, 1374–1389.

LIM, Z.L., CHONG, K.L., DING, G.-Y. & XIA, K.-Q. 2019 Quasistatic magnetoconvection: heat transport enhancement and boundary layer crossing. *J. Fluid Mech.* **870**, 519–542.

LOHSE, D. & SHISHKINA, O. 2023 Ultimate turbulent thermal convection. *Phys. Today* **76**, 26–32.

LOHSE, D. & XIA, K.-Q. 2010 Small-scale properties of turbulent Rayleigh–Bénard convection. *Annu. Rev. Fluid Mech.* **42**, 335–364.

MALKUS, W.V.R. & VERONIS, G. 1958 Finite amplitude cellular convection. *J. Fluid Mech.* **4**, 225–260.

MÜLLER, G., NEUMANN, G. & WEBER, W. 1984 Natural convection in vertical Bridgman configurations. *J. Cryst. Growth* **70**, 78–93.

PANDEY, A., KRASNOV, D., SCHUMACHER, J., SAMTANEY, R. & SREENIVASAN, K.R. 2022 Similarities between characteristics of convective turbulence in confined and extended domains. *Physica* D **442**, 133537.

REN, L., TAO, X., ZHANG, L., NI, M.-J., XIA, K.-Q. & XIE, Y.-C. 2022 Flow states and heat transport in liquid metal convection. *J. Fluid Mech.* **951**, R1.

ROCHE, P.-E., GAUTHIER, F., KAISER, R. & SALORT, J. 2010 On the triggering of the ultimate regime of convection. *New J. Phys.* **12**, 085014.

SCHINDLER, F., ECKERT, S., ZÜRNER, T., SCHUMACHER, J. & VOGT, T. 2022 Collapse of coherent large scale flow in strongly turbulent liquid metal convection. *Phys. Rev. Lett.* **128**, 164501.

SHISHKINA, O. 2021 Rayleigh–Bénard convection: the container shape matters. *Phys. Rev. Fluids* **6**, 090502.

VAN DER POEL, E.P., STEVENS, R.J.A.M. & LOHSE, D. 2011 Connecting flow structures and heat flux in turbulent Rayleigh–Bénard convection. *Phys. Rev.* E **84**, 045303.

VERZICCO, R. & CAMUSSI, R. 1997 Transitional regimes of low-Prandtl thermal convection in a cylindrical cell. *Phys. Fluids* **9**, 1287–1295.

WANG, Q., VERZICCO, R., LOHSE, D. & SHISHKINA, O. 2020 Multiple states in turbulent large-aspect-ratio thermal convection: what determines the number of convection rolls? *Phys. Rev. Lett.* **125**, 074501.

XIA, K.-Q. 2013 Current trends and future directions in turbulent thermal convection. *Theor. Appl. Mech. Lett.* **3**, 052001.

XIA, K.-Q., HUANG, S.-D., XIE, Y.-C. & ZHANG, L. 2023 Tuning heat transport via coherent structure manipulation: recent advances in thermal turbulence. *Nat. Sci. Rev.* **10**, nwad012.

XIE, Y.-C., CHENG, B.-Y.-C., HU, Y.-B. & XIA, K.-Q. 2019 Universal fluctuations in the bulk of Rayleigh–Bénard turbulence. *J. Fluid Mech.* **878**, R1.

XIE, Y.-C., WEI, P. & XIA, K.-Q. 2013 Dynamics of the large-scale circulation in high-Prandtl-number turbulent thermal convection. *J. Fluid Mech.* **717**, 322–346.

ZHANG, L. & XIA, K.-Q. 2023 Heat transfer in a quasi-one-dimensional Rayleigh–Bénard convection cell. *J. Fluid Mech.* **973**, R5.

ZHONG, J.-Q., STEVENS, R.J.A.M., CLERCX, H.J.H., VERZICCO, R., LOHSE, D. & AHLERS, G. 2009 Prandtl-, Rayleigh-, and Rossby-number dependence of heat transport in turbulent rotating Rayleigh–Bénard convection. *Phys. Rev. Lett.* **102**, 044502.

ZÜRNER, T., SCHINDLER, F., VOGT, T., ECKERT, S. & SCHUMACHER, J. 2019 Combined measurement of velocity and temperature in liquid metal convection. *J. Fluid Mech.* **876**, 1108–1128.

ZWIRNER, L., TILGNER, A. & SHISHKINA, O. 2020 Elliptical instability and multiple-roll flow modes of the large-scale circulation in confined turbulent Rayleigh–Bénard convection. *Phys. Rev. Lett.* **125**, 054502.